Journal of Controlled Release 360 (2023) 260–273

Contents lists available at ScienceDirect

Journal of Controlled Release

journal homepage: www.elsevier.com/locate/jconrel

Programmed T cells infiltration into lung metastases with harnessing dendritic cells in cancer immunotherapies by catalytic antigen-capture sponges

Min-Ren Chiang [a], Wei-Ting Shen [a,b], Pin-Xuan Huang [a], Kang-Li Wang [a], Wei-Han Weng [a], Chien-Wen Chang [a], Wen-Hsuan Chiang [c], Yu-Chen Liu [d,e], Shing-Jyh Chang [f,g], Shang-Hsiu Hu [a,*]

[a] Department of Biomedical Engineering and Environmental Sciences, National Tsing Hua University, Hsinchu 300044, Taiwan
[b] Department of Nanoengineering, University of California, San Diego, CA 92093, USA
[c] Department of Chemical Engineering, National Chung Hsing University, Taichung 402, Taiwan
[d] Laboratory for Human Immunology (Single Cell Genomics), WPI Immunology Frontier Research Center, Osaka University, Japan
[e] Center for Infectious Disease Education and Research (CiDER), Osaka University, Osaka, Japan
[f] Department of Obstetrics and Gynecology, Hsinchu Municipal MacKay Children's Hospital, Hsinchu 300, Taiwan
[g] Department of Nursing, Yuanpei University of Medical Technology, Hsinchu 300, Taiwan

ARTICLE INFO

Keywords:
Immunotherapy
Metal organic framework
Autophagy inhibition
Antigen capture
Immune checkpoint blockage

ABSTRACT

T lymphocytes served as immune surveillance to suppress metastases by physically interacting with cancer cells. Whereas tumor immune privilege and heterogeneity protect immune attack, it limits immune cell infiltration into tumors, especially in invasive metastatic clusters. Here, a catalytic antigen-capture sponge (CAS) containing the catechol-functionalized copper-based metal organic framework (MOF) and chloroquine (CQ) for programming T cells infiltration is reported. The intravenously injected CAS accumulates at the tumor *via* the folic acid-mediated target and margination effect. In metastases, Fenton-like reaction induced by copper ions of CAS disrupts the intracellular redox potential, *i.e.*, chemodynamic therapy (CDT), thereby reducing glutathione (GSH) levels. Furthermore, CQ helps inhibit autophagy by inducing lysosomal deacidification during CDT. This process leads to the breakdown of self-defense mechanisms, which exacerbates cytotoxicity. The therapies promote the liberation of tumor-associated antigens, such as neoantigens and damage-associated molecular patterns (DAMPs). Subsequently, the catechol groups present on CAS perform as antigen reservoirs and transport the autologous tumor-associated antigens to dendritic cells, resulting in prolonged immune activation. The CAS, which is capable of forming *in-situ*, serves as an antigen reservoir in CDT-mediated lung metastasis and leads to the accumulation of immune cells in metastatic clusters, thus hindering metastatic tumors.

1. Introduction

Lung neoplasms and metastases have been recognized as one of the deadliest types of cancer worldwide [1]. With the advancement of cancer treatment, various forms of cancer treatment have been implemented clinically, including surgery, radiotherapy, chemotherapy, immunotherapy, and antibody-targeted therapy. Recently, cancer immunotherapies have sprung up, which have the promising feature of triggering natural immune responses to fight cancer and prevent most of the side effects of conventional treatments [2]. However, the lack of cytotoxic T lymphocytes infiltrating into the deep core of solid tumors hampers the therapeutic efficacy of immunotherapy [3,4]. Especially in many metastases (typically <100 mm^3), poor vascularization exacerbates the dilemma of reduced physical activity of T cells and cancer cells in the early metastatic phase [5,6]. Immune privilege, which limits T-cell recognition and leads to evasion of T-cell attack, also occurs in limited activation of antigen-presenting cells (APCs) [7–9]. Therefore, the induction of tumor-specific T lymphocytes is the key to the immunotherapy of secondary tumor invasion.

One approach to enhance antigen immunogenicity is through the use

* Corresponding author.
E-mail address: shhu@mx.nthu.edu.tw (S.-H. Hu).

https://doi.org/10.1016/j.jconrel.2023.06.033
Received 22 February 2023; Received in revised form 22 May 2023; Accepted 22 June 2023
0168-3659/© 2023 Elsevier B.V. All rights reserved.

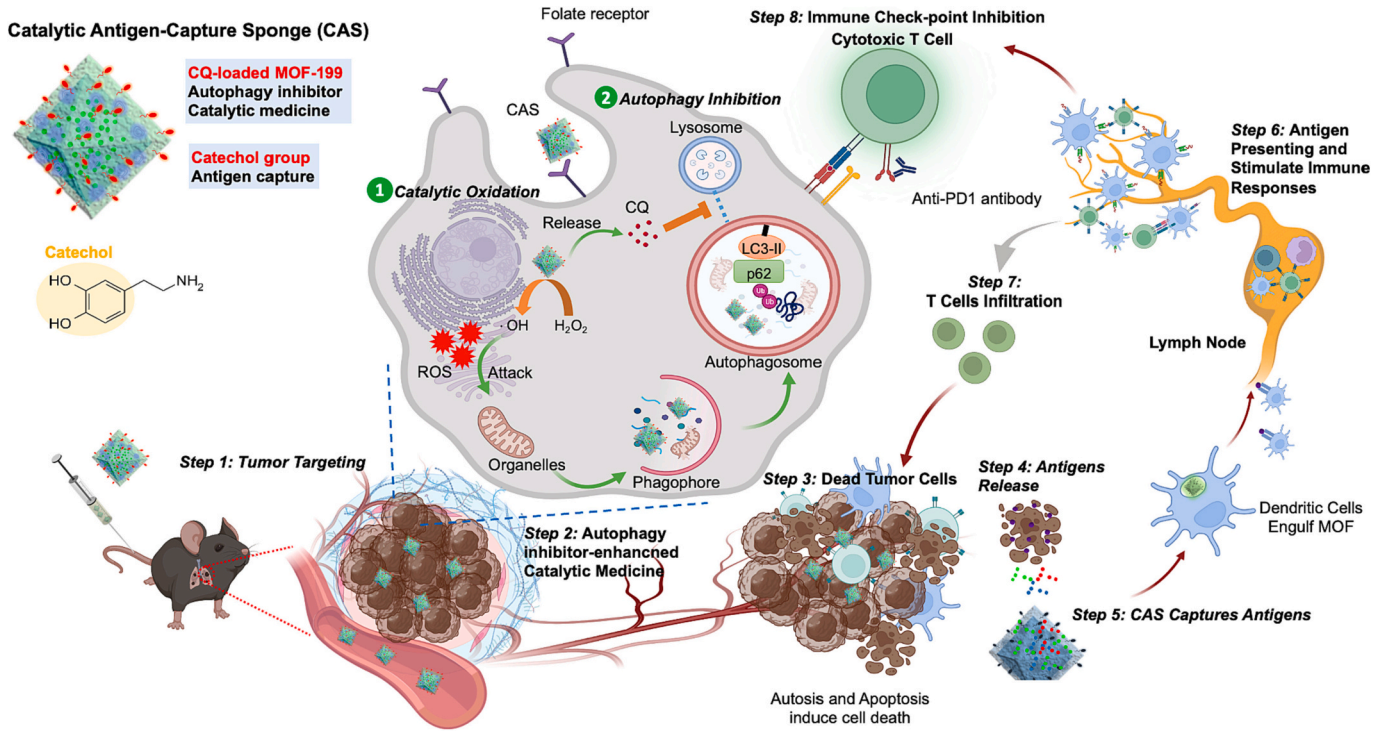

Fig. 1. The illustration of catalytic antigen capture sponges (CAS) acting as immunostimulants to enhance the efficacy of immunotherapy. CAS targets cancer cells through the folate receptor, which catalyzes oxidation and autophagy inhibition leading to cancer cell death and openings in solid tumor tissues, promoting T cell infiltration. Dendritic cells then present tumor antigens to activate T cells. The combination of CAS and immune checkpoint inhibitors improves the efficacy of eliminating cancer cells.

of immunogenic species [10–12]. An alternative approach is to utilize a delivery mechanism for conveying antigens to the lymph nodes and initiating antigen-specific interactions with T cells. This can be achieved through the use of tumor cell membranes, tumor lysates, or tumor cell exosomes that have been activated by epitopes produced by the tumor [13–15]. Although these approaches improve antigen presentation and antitumor immune responses, low immunogenicity remains a fundamental challenge [16,17]. Moreover, these strategies require complex procedures and preparations, and antigen transport may not effectively activate an immune response [6,18–21]. Despite advances in antigen retention by antigen-loaded gels and capture by functional groups and maleimides, presentation limitations may still impede successful immune responses [22–24].

The effectiveness of immunotherapy in treating metastases is hindered by low tumor-associated antigen presentation and the presence of a physiological barrier orchestrated by cancer-associated fibroblasts [25–27]. One strategy for improving tumor-associated antigens is to use hyperthermia *via* the high frequency magnetic field, which causes localized heating of the tumor to lysis the cell. This causes cell demise and damage *via* the activation of either the apoptosis or necrosis pathway. [28]. Another promising approach is chemodynamic therapy (CDT), which induces apoptosis in cancer cells by utilizing CDT reagents and Fenton reaction to generate reactive oxygen species (ROS) [5,29,30]. The Fenton reaction in CDT catalyzes the breakdown of H_2O_2 to produce highly reactive hydroxyl radicals (·OH) and hydroxide ions (OH^-) to induce oxidative stress, leading to apoptosis. This oxidative stress causes a range of cellular damage, including DNA damage, lipid peroxidation, and protein oxidation, that can further facilitate apoptosis [30,31]. Metal ions, such as Fe^{2+}, Cu^{2+}, or Mn^{2+}, as well as nanoparticles, are commonly used as CDT reagents to initiate the Fenton reaction [29,32]. However, one of the major obstacles in CDT therapy is the overexpression of glutathione (GSH) in cancer cells, which can lead to drug resistance. Therefore, engineering the tumor microenvironment and depleting GSH levels are critical for enhancing the effectiveness of CDT drugs [33,34].

Despite the recent CDT excitement, therapeutic agents such as metal-organic frameworks induce genotoxic responses and metabolic deficits [35], leading to the activation of autophagy, also known as a self-defense mechanism [36]. Modified MOFs have been documented as an effective strategy for mitigating autophagy activation in tumors. This approach aims to decrease the activation of autophagy within tumors [37,38]. These modified materials can be triggered by light or sound to carry out the Fenton reaction, using hydrogen peroxide and iron (Fe^{2+} and Fe^{3+}) to generate hydroxyl radicals. Furthermore, to inhibit autophagy, chloroquine (CQ) is used as a well-known inhibitor [39,40]. The downstream regulation of autophagy can be facilitated by activating receptors through innate immunity, which can enhance cytokine production and phagocytosis. In adaptive immunity, autophagy activation can promote the increase of antigen sources, resulting in direct cytotoxicity of $CD8^+$ T cells to cancer metastasis.

The *in-situ* depositing adherent nanogels can be administrated through intravenous injection and formed an adhesive gel upon a stimulus [33,41]. With the low systemic toxicity, the gel could reach the targeted site to release the therapeutic agents or execute the chemical reactions to elicit APCs [42,43]. Here, an *in-situ* depositing catalytic antigen-capture sponge (CAS) composed of chloroquine (CQ), copper-based metal organic framework (MOF), and polydopamine (PDA nanogels) for CDT-guided release of tumor-associated antigens and antigen capture (Fig. 1). Through folic acid (FA)-mediated targeting of lung metastasis, CAS acts as a programmed peroxide mimics in cancer cells, promoting sustained ROS generation. Inhibition of autophagy with the help of CQ regulates autophagic flux through obstruction of the fusion of autophagosome with lysosomes, reduces cancer cell self-defense mechanism then induces autosis cell death pathway and improves CDT efficacy [44]. The combined effect promotes the release of tumor-associated antigens (TAAs), which are then captured by catechol groups on CAS, leading to immunogenic cell death. Therefore, antigen capture by CAS has enormous potential applications in enhancing cancer

immunotherapy.

2. Materials and methods

2.1. Materials

Copper(II) nitrate trihydrate (Acros Organics, CAS Number: 10031–43-3), 1,3,5 benzenetricarboxylic acid (Alfa Aesar, CAS Number: 554–95-0), polyvinylpyrrolidone (Sigma-Aldrich, CAS Number: 9003-39-8), folic acid (FA, Sigma-Aldrich, CAS Number: 59–30-3), dopamine hydrochloride (DA salt, Acros Organics, CAS Number: 62–31-7), N, N- dimethylformamide (Honeywell, CAS Number: 68–12-2), dimethyl sulfoxide (Sigma-Aldric, CAS Number: 67–68-5), chloroquine diphosphate (Sigma-Aldrich, CAS Number: 50–63-5), L-glutathione reduced (Sigma-Aldrich, CAS Number: 70–18-8), hydrogen peroxide (Honeywell, CAS Number: 7722-84-1), methyl orange (Sigma-Aldrich, CAS Number: 547–58-0), 5,5′-dithiobis-(2-Nitrobenzoic Acid) (Sigma-Aldrich, CAS Number: 69–78-3)

2.2. Synthesis of MOF, FA-MOF, and PDA@MOF

The protocol for synthesizing MOF-199 (MOF) was adjusted from the previous report [45]. First, 0.29 g $Cu(NO_3)_2{\cdot}3H_2O$, 0.14 g 1,3,5 benzenetricarboxylic acid (BTC), and 0.1 g PVP were weighed and poured into centrifuge tubes, respectively. Then, 25 mL of DMF was added to tubes containing BTC and PVP. Another tube was prepared with 30 mL of DMF, which was loaded with $Cu(NO_3)_2{\cdot}3H_2O$. All three tubes were placed in a sonicator and subjected to 15 min of sonication. Then, three solutions were added and mixed into one pot. After 15 min, the solution in blue color was transferred into a Teflon container and then heated up to 80 °C for 14 h. The produced composite was collected *via* centrifugation at 12,000 rpm for 10 min, washed by DMF twice and EtOH twice individually, and placed into the oven at 60 °C for drying storage. For the synthesis of FA-modified MOF (FA-MOF), FA (0.055 g) was added during the solution preparation.

To coat PDA on the surface MOF, the process was based on previous approaches [46,47]. Basically, 0.1 g of MOF powders were re-dispersed into 20 mL of DMF. Then, 0.08 g of dopamine hydrochloride (DA salts) were added into the MOF-dissolved DMF solution and mixed for 6 h. The mixture would go for centrifuging and collecting in the condition of 12,000 rpm and 6 min with the wash of DMF once to remove residual DA molecules. After resuspending and scattering the remained MOF particles into 20 mL of DMF, the container was further soaked in the 75 °C water bath for 12 h for PDA coating formation. Finally, the products were gathered and washed with EtOH twice. The products were freeze-dried through the lyophilizer for storage in powder.

2.3. Preparation of catalytic antigen-capture sponge (CQ/FA-PDA@MOF)

Follow the previous study to bind FA adjuncts on PDA of MOF [48]. 0.1 g of PDA-coated MOF was weighed in the container, and dissolved in 10 mL of PBS buffer. Afterward, another solution was prepared by the addition of 0.03 g of FA powder into 3 mL of DMSO, and 1 mL of this mentioned DMSO solution was injected into the stirring PDA-modified MOF-loaded solution stirring for 2 h. The evenly mixed solution was then kept stationary for another 2 h, washed by 50% EtOH three times, and the outcomes, FA-PDA@MOF, were freezing-dried *via* the lyophilizer for preservation in the solid state.

To prepare CQ/FA-PDA@MOF, 0.005 g of CQ was added to 20 mL of DMF containing 0.1 g of MOF, and the mixture was stirred overnight. The CQ-loaded products were then centrifuged at 12,000 rpm to remove the supernatant and resuspended in 20 mL of DMF for further PDA coating and FA conjugation. The resulting CQ/FA-PDA@MOF is a catalytic antigen-capture sponge (CAS).

2.4. The material functionality characterization

The Fenton-like reaction and GSH depletion ability for MOF were determined as follows. GSH levels were determined using a color-change indicator, 5,5′-dithiobis-(2-nitrobenzoic acid) (DTNB). At first, 10 mM of DTNB dissolved in pH 7.4 phosphate buffer; afterward, 100 μL of 40 mM GSH, 100 μL of 2 mg/mL MOF, 160 μL of purified water, and 40 μL of pH 7.4, phosphate buffer were mixed for a 3-h reaction after the adjustment of pH value of the mixture into pH 5.0 and pH 7.4 by adding 10 mM of NaOH solution for mimicking the intracellular lysosome and tumor microenvironment, respectively; later, the mixture was centrifuged to remove MOF and the UV–vis spectra of each sample were measured.

In the context of ROS generation primed by the reaction between MOF and hydrogen peroxide, methyl orange (MO), was picked up as the excellent ROS-responsive color indicator for demonstrating the copper-ion-induced Fenton-like reaction elicited by produced MOF. Then, UV–vis spectra were measured to determine the level of ROS. For the cellular ROS determination, the ROS kit (Abcam, ab219931) was used and followed the manufacturer's procedure for staining. After that, the confocal images were taken, and using ImageJ to analyze the fluorescence intensity.

2.5. Cytotoxicity, distribution, and cellular uptake of MOF

B16F10 (murine melanoma tumor cell line) was purchased from Food Industry Research and Development Institute and the B16F10 carrying GFP-P2A-NanoLUC expression vector cell line was obtained from Professor Chang CW, Department of Biomedical Engineering and Environmental Sciences, National Tsing Hua University, Hsinchu. The cells were cultured in Dulbecco's modified eagle medium (DMEM) with 10% fetal bovine serum and 1% penicillin/streptomycin in a 5% CO_2-enriched environment at 37 °C.

10^5 cells/mL of cells were added into 96-well microplates. After 24 h incubation, the various MOF in specific conditions was resolved in completed culture medium and co-culture with cell for an additional 24 h. Eventually, the PrestoBlue cell viability reagent (Thermo, A13261) was added to each well according to the manufacturer's procedure to develop signals. Then, the fluorescence signal was obtained by the microplate reader. The non-treated control was considered as 100% viability for each run of the assay.

MOF were labeled with Cy5.5 Amidite dye (Cytivia, 28,904,250). As the first step, 10^5 cells/ mL of cells were added into poly-L-lysine coated coverslips and cultured for 24 h. Afterward, various labeled MOF were added and cultured for designed periods. At the end of the assay, the cells were fixed by 3.7% formaldehyde and permeabilized by 0.1% Triton-X100. DAPI and phalloidin (Invitrogen, A12379) were added to stain the nucleus and F-actin, respectively. Then, confocal laser scanning microscope (Zeiss LSM800) images were taken.

To quantify the uptake of nanoparticles, B16F10 cells were seeded into 6-well culture plates at a density of 2×10^5 cells per well. After incubation for 24 h, various Cy5.5 labeled MOF were added to the well for different experimental conditions. The cells were harvested by trypsin-EDTA treatment and resuspended in PBS buffer. Finally, flow cytometry (Attune NxT) was used to analyze uptake situations and the data were evaluated by FlowJo software (Tree Star), to quantify the amount of particle uptake by cells (accumulating 10,000 events).

2.6. Autophagy performance test

10^5 cells/mL of B16F10 cells were prepared. After 24 h of medium culturing and an hour of PBS starvation, cells were treated with various MOF conditions for additional 24 h. Then, PBS buffer containing 1% BSA, 10% goat serum, 0.3 M glycine, and 0.1% Tween-20 was prepared and added to each sample for 1 h. 500-fold diluted LC3B (Abcam, ab192890) and p62 (Irealbio, IR91–394) primary antibodies were prepared with the blocking buffer and added to every sample for 16 h at

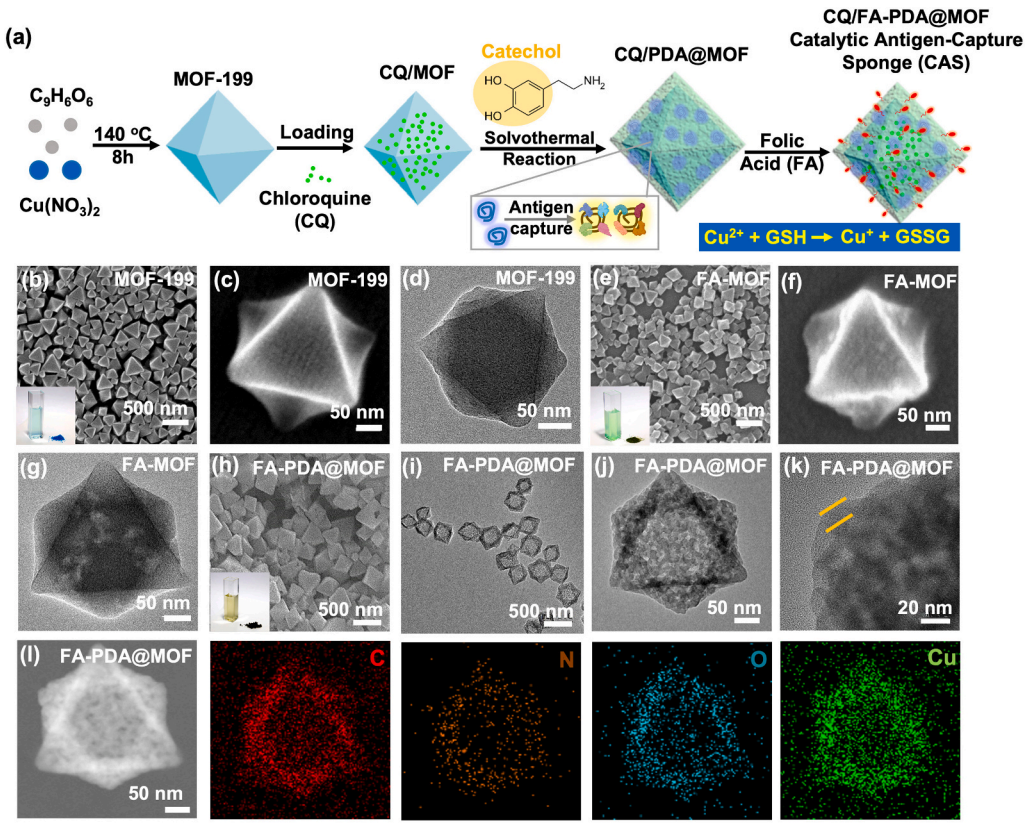

Fig. 2. Synthesis and characterizations of the MOF. (a) The schematic illustration of the synthetic process of the CQ/FA-PDA@MOF. SEM image of (b,c) MOF, (e,f) FA-MOF, and (h) FA-PDA@MOF. TEM images of (d) MOF, (g) FA-MOF, and (i-k) FA-PDA@MOF. (l) Elemental mapping of FA-PDA@MOF.

4 °C conditions. Washed by PBS buffer, the corresponding 500-fold diluted secondary antibodies (Abcam, ab150075; Jackson, AB2340621) dissolved in the blocking buffer were added and incubated for 1 h. Finally, the antibody solution was moved out and stained with phalloidin; then, mounting with DAPI mounting media.

2.7. *In vivo biodistribution study*

The lung metastasis model was built upon the female C57BL/6 mice with the age range of 8–10 weeks old which were purchased from Bio-LASCO Co., Ltd. To establish the tumor-bearing mice model, 5×10^5 of GFP-P2A-NanoLUC B16F10 cells were inoculated to mice *via* tail veins intravenous injection.

After 13 days of inoculation, the doxorubicin-labeled MOF were injected into the mice *via* intravenous injection. On the next day, the mice were sacrificed, and perfusion of 15 mL of 4% paraformaldehyde solution as well as 15 mL PBS buffer. The biodistribution images were taken by IVIS (PerkinElmer, IVIS Spectrum *in vivo* imaging system); then, the lung tissues were further fixed with 4% PFA overnight at 4 °C.

Afterward, immunohistochemistry staining was conducted on lung sections. 200-fold diluted anti-CD31 primary antibody (BD Pharmingen, 550,274) and 200-fold diluted secondary antibody (Abcam, ab150075) were used to label CD31 on the normal endothelial cells. The CLSM images were taken with these samples for evaluation of nanoparticle distribution within lung tissues.

2.8. *Dendritic cells induced immune response in lymph node*

After B16F10 cells inoculated for 13, 16, and 19, Cy5.5 labeled MOF were injected *via* intravenous injection. After 22 days of inoculation, mice were sacrificed and neck lymph nodes were taken and fixed. Then, 1000-fold diluted CD11c (Abcam, ab219799), and CD80 (Abcam, ab62636) primary antibodies and 1000-fold diluted secondary antibodies (Abcam, ab150081, ab150160) were used to stain the dendritic cells. The CLSM images were taken to evaluate the co-localization of MOF and dendric cells.

2.9. *In vivo analysis of T lymphocytes-associated immune responses*

The GFP-B16F10 tumor-bearing mice were established as previous process. The MOF were treated on day 13, 16, and 19 after tumor inoculation. After 22 days of inoculation, mice were sacrificed and lung tissues were fixed and stained with 200-fold diluted anti-CD8 primary antibody (Abcam, ab217344) and 500-fold diluted secondary antibody (Abcam, ab150075). The CLSM images were taken to evaluate the location of CD8+ cells and tumor cells.

2.10. *Flow cytometry for cytotoxic T and helper T cells analysis*

Flow cytometry is utilized for quantifying the MOF treatment-primed immune responses within lung metastasis. The isolated lung tissues were digested by 0.1 mg/mL collagenase solution (Sigma, C0130), 1 μg/mL DNase solution (Sigma, DN25), and 6.6 μg/mL dispase I solution (Sigma, D4818) in HBSS buffer (Sigma, H8264) for 50 min in room temperature and then, filtered through transferring tissue solutions to 70 μm cell strainers. To prevent the non-specific binding, 50 μL goat serum and 10 μL Fc Blocker (BD Pharmingen, 553,142) were added to samples at room temperature for 50 min.

Later, the blocked cell solution was then divided into several flow tubes for immune cell labeling. In terms of the addition of antibodies, PE/Cyanine7 anti-mouse CD45 antibody (Biolegend, 103,114, dilution ratio: 1:500), FITC anti-mouse CD3ε antibody (Biolegend, 100,306, dilution ratio: 1:500), PE anti-mouse CD4 antibody (Biolegend, 100,408, dilution ratio: 1:500) and APC anti-mouse CD8a antibody (Biolegend,

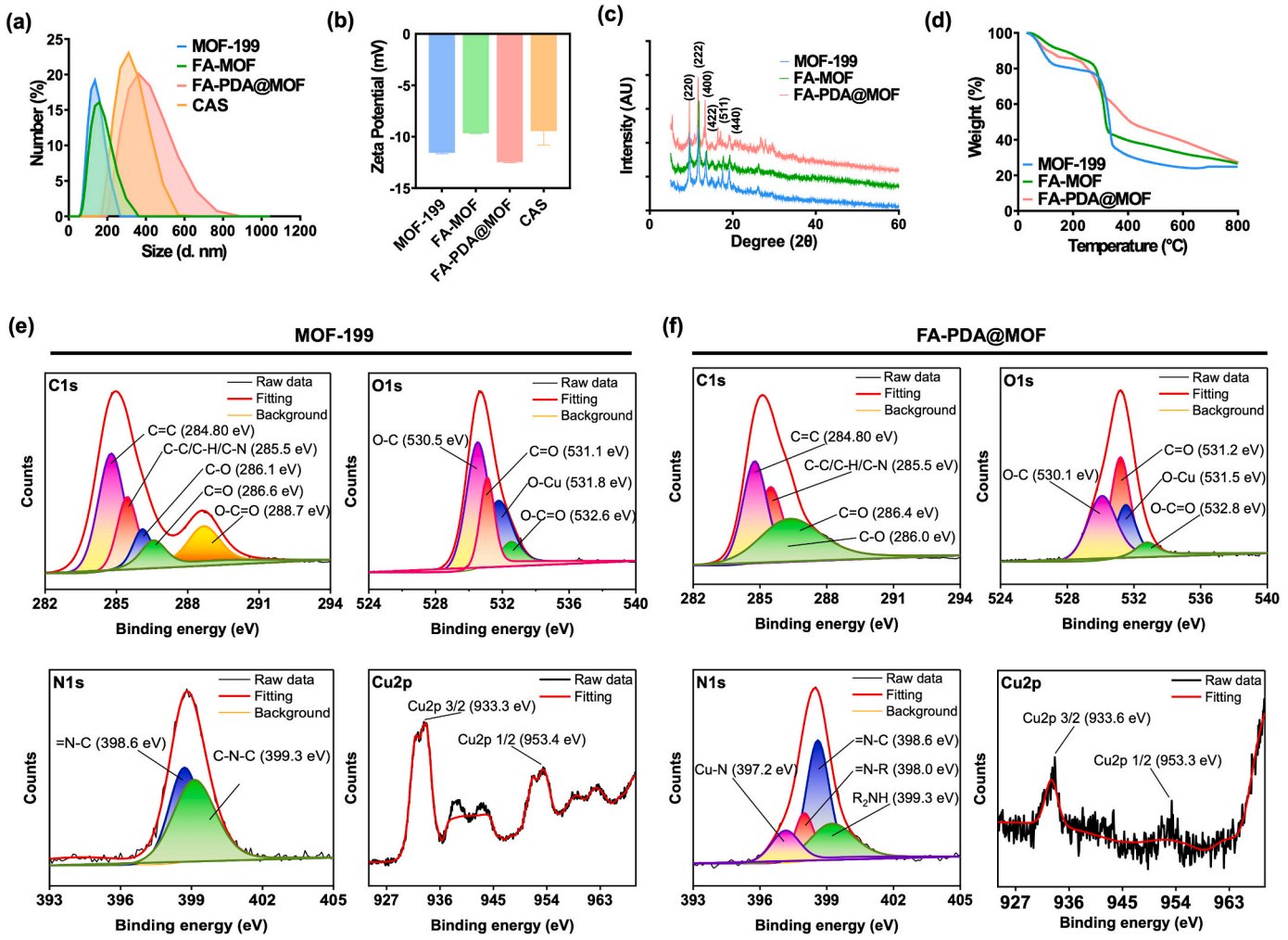

Fig. 3. Physicochemical characterization of MOF, FA-MOF, and FA-PDA@MOF. (a) Size distributions, (b) Zeta potential, (c) X-ray diffraction spectrum, and (d) Thermogravimetric analysis of MOF, FA-MOF, and FA-PDA@MOF. (e-f) XPS spectrum of all the elements of MOF and FA-PDA@MOF.

100,712, dilution ratio: 1:500) were utilized to label targeting immune cells. After the antibody dying in the dark icebox for 30 min, flow tubes loaded with labeled cell solution would be centrifuged with the rotation condition of 1550 rpm for 5 min, and cells would be resuspended into 1 mL iced PBS buffer. Finally, samples were used flow cytometry to analyze the ratio of cytotoxic T and helper T cells in the lung.

For flow data processing, the following steps were conducted. First of all, the compensation sets were tested as the negative control, and the gating strategy of obtained flow data was thus determined, respectively establishing the intensity standard of positive fluorescence ranges after tuning machinery parameters. Besides, the gating region in the FSC-SSC plot was adjusted and then fixed to circle the group of lymphocytes and to exclude noises from other cells [49].

2.11. *In vitro antigen capture studies for catalytic antigen-capture sponge (CAS)*

In the beginning, 10^5 B16F10 cells had been seeded into a 6-well plate. After two days of culture, the culture medium will be changed to serum free medium for an additional day culture and followed by adding CAS to kill the cells. Then, the cell supernatant was collected, and used 3 k concentrator to remove the residual drugs and culture medium. Next, CAS were added to the supernatant to examine the antigen capture ability. Finally, the protein-bound CAS particles were spun down and run an SDS-PAGE. The Coomassie blue stained band were cut out and sent to National Taiwan University Consortia of Key Technologies and Instrumentation Center for liquid chromatography/tandem mass spectroscopy (LC/MS/MS) analysis. Neoantigen proteins in B16F10 cell line were identified from previous reports [50–52]. Protein class analysis utilized Panther for analysis.

2.12. *In vivo efficacy studies in mice*

The B16F10 tumor-bearing mice were established as previous process. After 6, 9, and 12 days of tumor inoculation, MOF were injected *via* intravenous injection. For the immune therapy groups, anti-PD1 antibodies were administered to mice after 7, 10, and 13 days of tumor inoculation. On day 14, mice were sacrificed and tumor nodules were counted under the dissecting microscope.

3. Results and discussion

3.1. *Synthesis and characterization of CAS*

The synthesis process of CAS composed of chloroquine (CQ), copper-based metal organic framework (MOF), and polydopamine (PDA nanogels) is depicted in (Fig. 2a). Initially, MOF was synthesized through the hydrothermal method, utilizing Copper (II) Nitrate Trihydrate and 1,3,5 Benzenetricarboxylic Acid (BTC). Subsequently, chloroquine (CQ) was loaded onto the porous structure of MOF *via* the π–π interactions and van

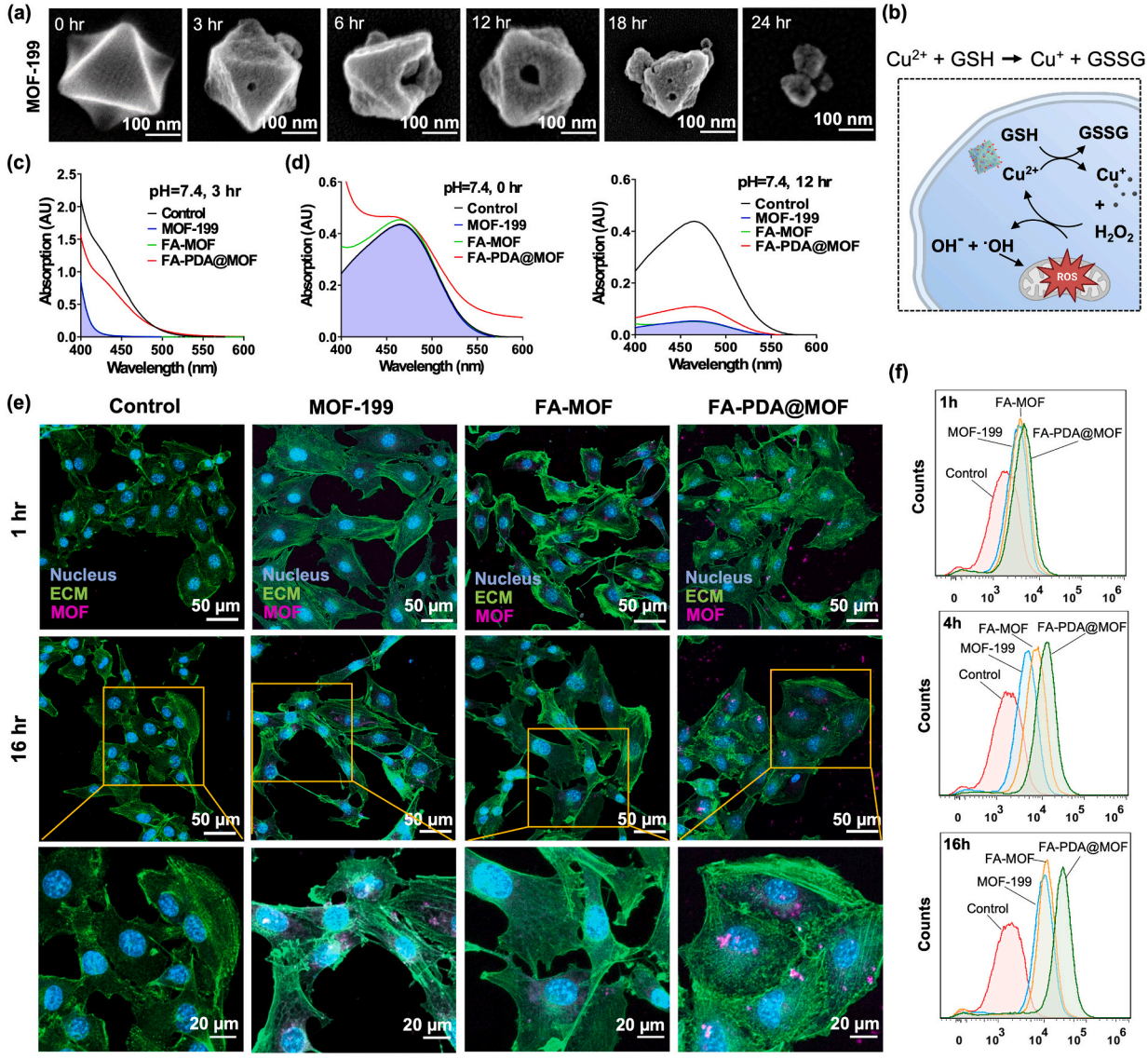

Fig. 4. Hydrolysis and *in vitro* cancer cells targeting capability of MOF. (a) SEM images of MOF hydrolysis process exposure in water. (b) The illustration of CAS hydrolysis and Fenton-like reaction process. (c) The UV–vis spectra change of GSH-responsive DTNB agents in pH 7.4 neutral situation. (d) The UV–vis spectra change of ROS-responsive methyl orange agents in pH 7.4 neutral situation after 12 h incubation. (e) Time-dependent cellular uptake images and (f) the quantification of flow cytometry results.

der Waal forces, followed by the coating of dopamine through a solvothermal reaction, to obtain CQ/PDA@MOF [5]. Based on previous literature, CQ has a peak absorption at 340 nm (Fig. S1) [53]. In order to determine the encapsulation efficiency of the drug, the supernatant of the loading solution was collected *via* centrifugation, resulting in an encapsulation efficiency of approximately 75%. The morphology of MOF, FA-MOF, FA-PDA@MOF, and CAS were characterized by scanning electron microscopy (SEM) and transmission electron microscopy (TEM) (Fig. 2b–k, S2). The results showed that all particles existed in uniform size and shape. Subsequent surface modifications did not affect the morphology uniformity. After the sequential coating of PDA and FA, the designed FA-PDA@MOF exhibits brown color and retains the original octahedral shape with obvious polymer coating, as shown in the TEM images (Fig. 2i–j). The PDA is rich in active functional groups, such as catechol, amine, and imine groups, which facilitate its coating onto the copper surface [54]. TEM images also indicated the presence of PDA shells on the MOF particles (Fig. 2k). It should be noted that for all three types of MOF, elemental mapping signals of copper, oxygen, carbon, and nitrogen were detected at some level (Fig. 2l). The copper signal is from the MOF, while the carbon and oxygen signals are from the MOF or components used for polymer surface modification. Regarding the nitrogen signals, PDA and FA are believed to provide most of the signals for the FA-MOF and FA-PDA@MOF nanoplatforms.

In this study, we employed dynamic light scattering to evaluate the physical characteristics of MOF-based nanomaterials, specifically focusing on particle size and surface charge (Fig. 3a,b). Our findings demonstrate that the introduction of surface modifications led to an increase in MOF size, from 250 nm to 300 nm. It is worth noting that all MOF products exhibited a negative surface charge, which is advantageous in preventing cellular uptake in negatively charged cell membranes. However, we observed that the incorporation of carboxyl-containing FA molecules resulted in a loss of BTC compounds, leading to reduced negative surface charges in FA-MOF formulations. Furthermore, FA-PDA@MOF displayed the most negative surface charge due to the high retention of carboxyl groups in MOF, PDA, and FA components.

To investigate the crystallization of particles, X-ray diffraction (XRD) analysis was conducted (Fig. 3c). The diffraction peaks detected at 9.5°, 11.7°, 13.5°, 16.5°, 17.5°, and 19.1° represented the standard markers

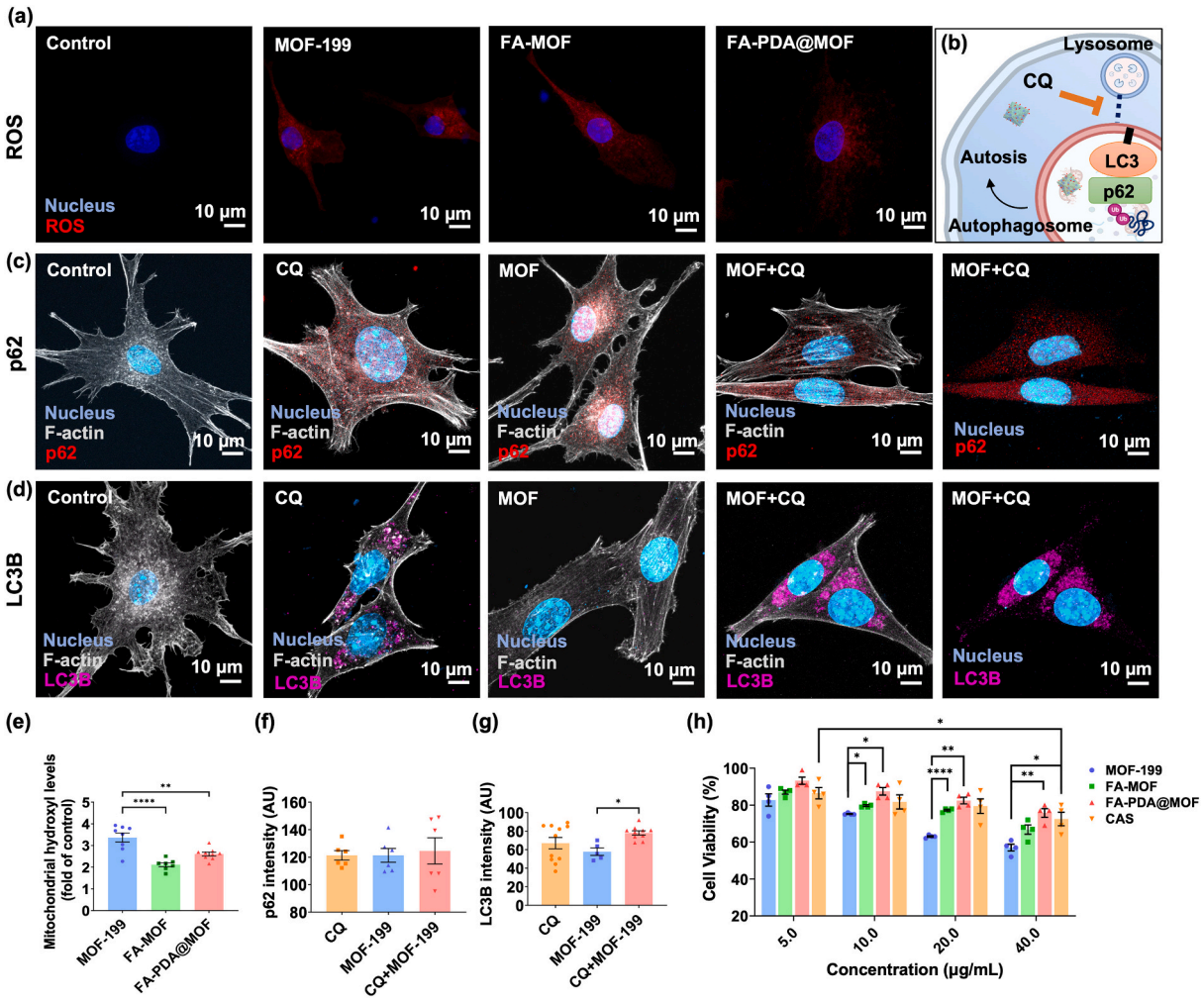

Fig. 5. *In vitro* cellular assay for ROS generation, autophagy inhibition, and cytotoxicity evaluation. (a) The mitochondrial hydroxyl radical ROS generation with the stimulus MOF. (b) The illustration of CQ function in autophagy inhibition. (c) The intracellularly autophagic p62 accumulation with the stimulus of particles. (d) The intracellularly LC3B-expressed autophagosome accumulation with the stimulus of CQ. (e) Quantitative mitochondrial hydroxyl levels are expressed as the percentage of hydroxyl identified in control cells. Statistical significance was assessed using one-way ANOVA. Data represent mean ± SEM (f) p62 relative fluorescence intensity. Statistical significance was assessed using one-way ANOVA. Data represent mean ± SEM (g) LC3B relative fluorescence intensity. Less fluorescence was detected in the control cells. Statistical significance was assessed using one-way ANOVA. Data represent mean ± SEM (h) Cell viability testing in B16F10 of MOF treatment. Statistical significance was assessed using two-way ANOVA. Data represent mean ± SEM, Asterisk represents significance values. $^{*}p < 0.05$, $^{**}p < 0.01$, $^{***}p < 0.001$, $^{****}p < 0.0001$.

of MOF, signifying crystal planes (220), (222), (400), (422), (511), and (440), respectively. These findings indicate that MOF possessed a face-centered cubic crystal lattice [69,70]. Furthermore, all particles exhibited these four peaks in their XRD spectra, indicating that their crystalline structure remained intact despite undergoing modifications with PDA and FA. Additionally, we observed a bump in the XRD spectrum of FA-PDA@MOF within the angle range of 20° to 30°, which corresponds to the characteristic peaks of PDA materials previously reported [71].

Thermogravimetric analysis (TGA) and X-ray photoelectron spectroscopy (XPS) were applied to understand organic/inorganic ratios and bonding. TGA analysis revealed two major weight losses of the MOF at 100 °C and 300 °C. The former represents the removal of residual or attached water or solvent molecules adsorbed on the inner or outer surfaces, and the latter represents the thermal decomposition of the octahedral framework (Fig. 3d). The curves obtained from FA-MOF maintained a higher residual weight due to the addition of folic acid. However, the curve of FA-PDA@MOF showed a larger residual weight but a smoother weight loss. Based on prior studies, the findings indicate the successful conjugation of FA and PDA through π-π interactions and hydrogen bonding [55].

XPS analysis in Fig. 3e,f showed that the Cu 2p spectra of MOF and FA-PDA@MOF have two distinct peaks at 933.3 eV and 953.4 eV, representing the Cu framework [56]. However, after deconvoluting the spectrum of FA-PDA@MOF, the Cu signal was greatly attenuated due to the polymer coating of PDA. Previous studies have reported that the C 1 s spectrum of MOF displays peaks at 284.80 eV, 285.5 eV, 286.1 eV, 286.6 eV, and 288.7 eV, corresponding to C═C, C-C/C-H/C-N, C—O, C═O, and O-C=O bonds [57]. The O 1 s spectrum for MOF shows peaks at 530.5 eV, 531.1 eV, 531.8 eV, and 532.6 eV, respectively corresponding to O—C, C═O, O—Cu, and O-C=O bonding [58]. The N 1 s spectrum of FA-PDA@MOF exhibited four peaks, which were fitted at 397.2 eV (Cu—N), 398.6 eV (=N-C), 398.0 eV (=N-R), and 399.3 eV (R_2NH), with the peaks at 398.0 eV (=N-R) and 399.3 eV (R_2NH) attributed to polydopamine [59,60]. Furthermore, the significant shift of the C═O signal from the carbon spectrum range to the oxygen spectrum region confirmed the successful PDA binding and FA conjugation, consistent with previous studies [61,62].

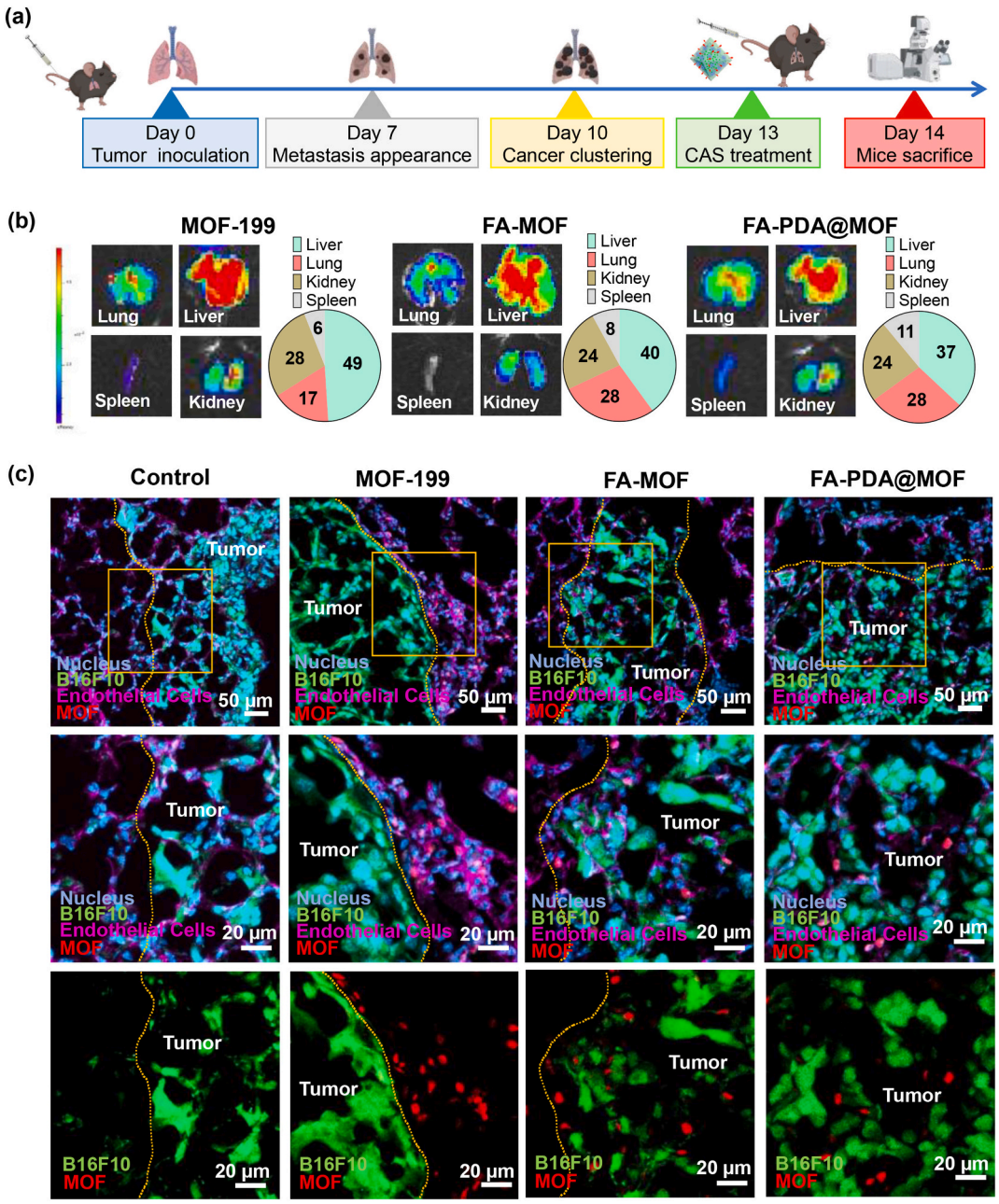

Fig. 6. (a) The tumor inoculation process for lung metastasis animal modeling. (b) IVIS fluorescence images displaying the MOF biodistribution. (c) Immunofluorescence images of lung metastatic tumor models treated with MOF.

3.2. Nitrogen adsorption-desorption isotherms of MOF, FA-PDA@MOF

The surface area of various particles was evaluated by analyzing the nitrogen adsorption-desorption isotherms using the BET method (Fig. S3). Based on the type IV isotherm observed in the analysis, MOF exhibited the characteristic of materials with mesoporous properties. However, the presence of macropores arising from the gaps between the accumulated MOFs, which are evident above relative pressures of 0.4 with some gaps extending beyond relative pressure values of 0.8 [63]. FA-PDA@MOF showed similar result curves but with lower mesoporosity. This result indicated that PDA filled the surface cavities or internal pores. FA-PDA@MOFs are considered capable of delivering small-molecule drugs because of their appropriate porosity and pore size.

3.3. Hydrolysis and redox imbalance of MOF

The hydrolytic ability and redox imbalance ability of nanoparticles are closely related to biocompatibility and cytotoxicity [64]. After 24 h of exposure to water, the MOF was observed to collapse from octahedral faces to the entire structure. The hydrolysis is attributed to thermodynamic reasons and the decomposition of paddle wheel subunits of MOF [65]. This observation suggests the possible release of intrinsic copper ions and unloading of the carried CQ molecules (Fig. 4a).

To assess the copper ion-induced Fenton reaction mediated by MOF, GSH depletion and ROS generation were evaluated in aqueous solutions with varying pH values (Fig. 4b–d). The ability of MOF, FA-MOF, and FA-PDA@MOF to consume GSH and form GSSG in an acidic pH 5.0 phosphate buffer environment is determined by the color change of the DTNB indicator and the peak reduction on the UV–Vis spectrum (Fig. S4a, b). Although FA-PDA@MOF required a longer time to

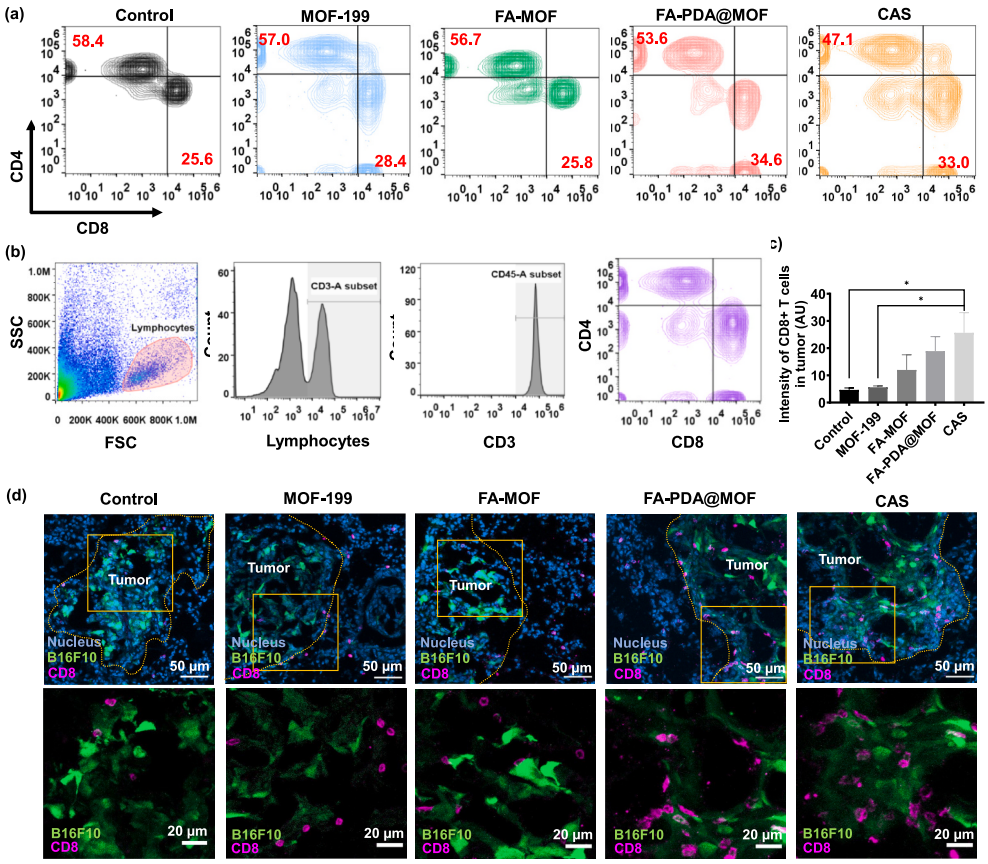

Fig. 7. *In vivo* immune response study. (a) The flow cytometry plots exhibit different groups of T lymphocytes that existed in lung tissues isolated from 14-day tumor-bearing mice with the administration of MOF. (b) Gating strategy of T lymphocytes in flow cytometry. (c,d) Immunofluorescence images of lung metastatic tumor models treated with MOF and stained with $CD8^+$ T cell marker. Quantitative fluorescence intensity of $CD8^+$ T cells in the tumor. The CAS shows excellent tumor infiltration ability. Statistical significance was assessed using one-way ANOVA. Data represent mean ± SEM.

completely deplete GSH molecules in neutral pH 7.4 phosphate buffer compared to MOF and FA-MOF, the three types of MOFs showed similar depletion of GSH ability (Fig. 4c). This data demonstrates that the PDA coating imparts pH-responsive properties to the nanoparticles, which provides important protection against leakage of copper ions or exposure of the copper-filled surface during the *in vivo* circulation of the nanoparticles. Furthermore, the colloidal stability of MOFs in ethanol and PBS had also been conducted (Fig. S5). The size and surface charges of the MOFs remained relatively unchanged under the specific conditions.

In the methyl orange ROS generation assay, a similar trend was observed for the three MOFs in their ability to induce ROS generation. A decrease in UV–Vis peak intensity was detected in acidic pH 5.0 phosphate buffer solution. However, in neutral pH 7.4 phosphate buffer solution, compared with MOF and FA-MOF, FA-PDA@MOF showed weaker ROS generation, slower color decay rate, and continuous decrease of UV–Vis absorption. As reported in previous studies, the pH-responsive properties were associated with and induced by tertiary amines on dopamine derivatives used for PDA coatings [66]. This result demonstrates that the pH-responsive PDA coating can prevent acute ROS generation in blood circulation (Fig. 4d).

3.4. *In vitro cellular uptake of MOF*

To assess the cellular uptake capacity of MOFs, different formulations of MOFs were treated at different times. Confocal images and flow cytometry reveal time-dependent cellular uptake (Fig. 4e–f). Under the same treatment conditions, the observed phagocytosis of FA-PDA@MOF was the highest among the three formulations. Meanwhile, the absorption concentration of FA-MOF is higher than that of MOF. This observation corresponds to previously reported experiments in which surface binding of FA induces folate receptor-mediated internalization, whereas biocompatible PDA coatings induce folate receptor-mediated internalization through various mechanisms such as energy-dependent phagocytosis and micropinocytosis [67]. Additionally, charge-associated interactions between B16F10 membranes and PDA-presenting positive amino groups with cytomembrane-existing negative phosphate complexes may also contribute to enhanced uptake [68].

3.5. *MOF induce intracellular ROS generation*

After assessing the cellular uptake capacity, the different particles were assessed for their ability to perform copper-based Fenton-like responses and intracellular ROS induction (Fig. 5a, b, e). The results showed that all three MOFs efficiently triggered the copper ion Fenton-like reaction, resulting in a significant hydroxyl radical signal. Notably, the ROS signal intensity in the unmodified MOF was significantly higher than in the other formulations due to the rapid hydrolysis of the copper backbone. The results of the combined cell and methyl orange ROS assays indicated that the FA and PDA coatings prevented the acute cytotoxicity of copper ions and instead resulted in the sustained production of ROS in cancer cells.

3.6. *Synergistic MOF and chloroquine (CQ) on autophagy regulation*

To assess the potential synergy of MOF catalysis and autophagy inhibition in cancer therapy, two autophagy-specific biomarkers, LC3B protein, and p62 complex, were evaluated and quantified under CLSM [69,70]. Results showed that p62 signaling was expressed in all treatment groups, suggesting that CQ or MOF activated intracellular autophagy (Fig. 5b, c, f). LC3B signaling was less induced by MOF but significantly increased in the free CQ and dual combination treatment groups, suggesting inhibition of lysosome-autophagosome fusion and autophagosome accumulation to enhance intracellular stress (Fig. 5b, d,

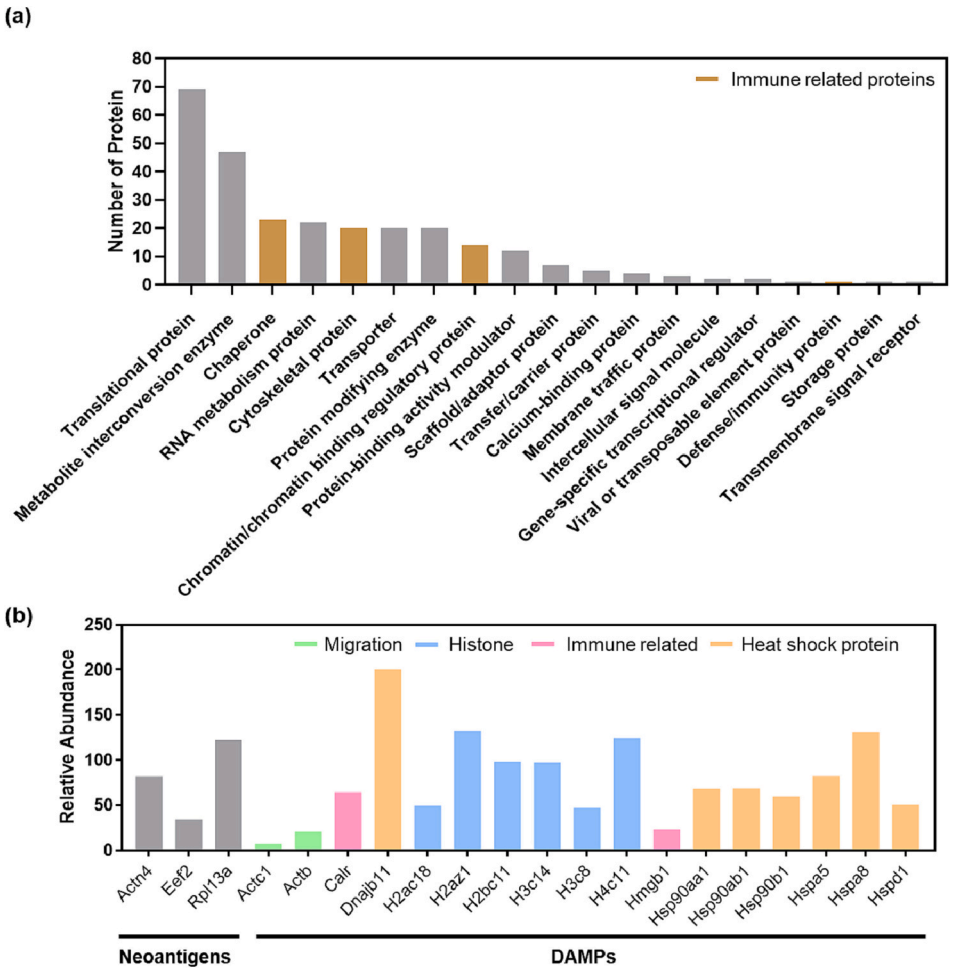

Fig. 8. (a) The identified proteins represent different classes of proteins. (b) The neoantigens and DAMPs captured by CAS.

g). These results demonstrated the feasibility of combinational therapy with MOF and CQ.

3.7. Cytotoxicity of MOF in cancer cells

The cytotoxicity of different MOF formulations was evaluated in the B16F10 cell line and found that cytotoxicity increased with the dose of all three MOF formulations (Fig. 5h). The cell viability was highest in the FA-PDA@MOF treatment group, followed by the FA-MOF application group, then MOF, and then the CQ/FA-PDA@MOF participation group. This is due to the lower ratio of copper and more polymer modifications in MOF at the same weight concentration, as well as the remarkable anti-tumor cytotoxicity provided by CQ for the whole MOF nanomedicine. These findings corroborate the results of acute ROS accumulation and autophagy inhibition.

3.8. In vivo biodistribution of MOF

In vivo animal models are used to understand the biodistribution of MOFs. Thirteen days after tumor inoculation, MOFs were injected intravenously into tumor-bearing mice (Fig. 6a). After harvesting of major clearing organs, IVIS analysis shows particle accumulation *in vivo* (Fig. 6b). FA-MOF exhibited higher accumulation in lung tumors due to reduced charge-attraction-induced uptake and enhanced permeability and retention effects in normal cells [71]. FA linked to MOFs can enhance internalization of targeted metastases through folate receptor (FR)-mediated endocytosis. Folate receptor is overexpressed in many tumor cells, including ovarian, and lung tumors, but not in normal cells [72]. Immunofluorescence staining analysis and flow cytometry analysis showed that FA provided excellent tumor targeting (Fig. 6c, S7). FA@MOF and FA-PDA@MOF facilitated deeper penetration into solid tumor tissues. Flow cytometry analysis revealed that the majority of FA-modified MOFs accumulated in the tumor area rather than in the blood vessels (Fig. S7). Without assistance of FA, MOF alone was mainly retained in tumor tissues exterior or surface.

3.9. MOF induce the infiltration of cytotoxic T lymphocytes

The induction of intracellular reactive oxygen species (ROS) by CDT can promote immunogenic cell death (ICD) in cancer cells [73]. However, increased ROS production leads to the activation of autophagy, also known as a self-defense mechanism [36]. In this regard, chloroquine (CQ) was used as a well-known inhibitor that promotes the downstream regulation of autophagy through innate immune activation receptors to exacerbate cancer cell death [74]. In this study, flow cytometry was used to investigate the expected priming of immune responses, particularly the populations of $CD8^+$ cytotoxic T lymphocytes and $CD4^+$ helper T lymphocytes (Fig. 7a, b). As the results showed, only the cytotoxic T cell population exhibited a slight increase with the CAS and FA-PDA@MOF formulations (Fig. 7a, S8).

To further explore the interaction between tumor cells and T lymphocytes, immunofluorescence staining was used to analyze the localization of $CD8^+$ T cells and assess their ability to penetrate the tumor. Infiltration of $CD8^+$ T cells at tumor sites was lower for MOF and FA-MOF but higher for FA-PDA@MOF and CAS containing PDA, suggesting a critical role of PDA in attracting and accumulating more $CD8^+$ T

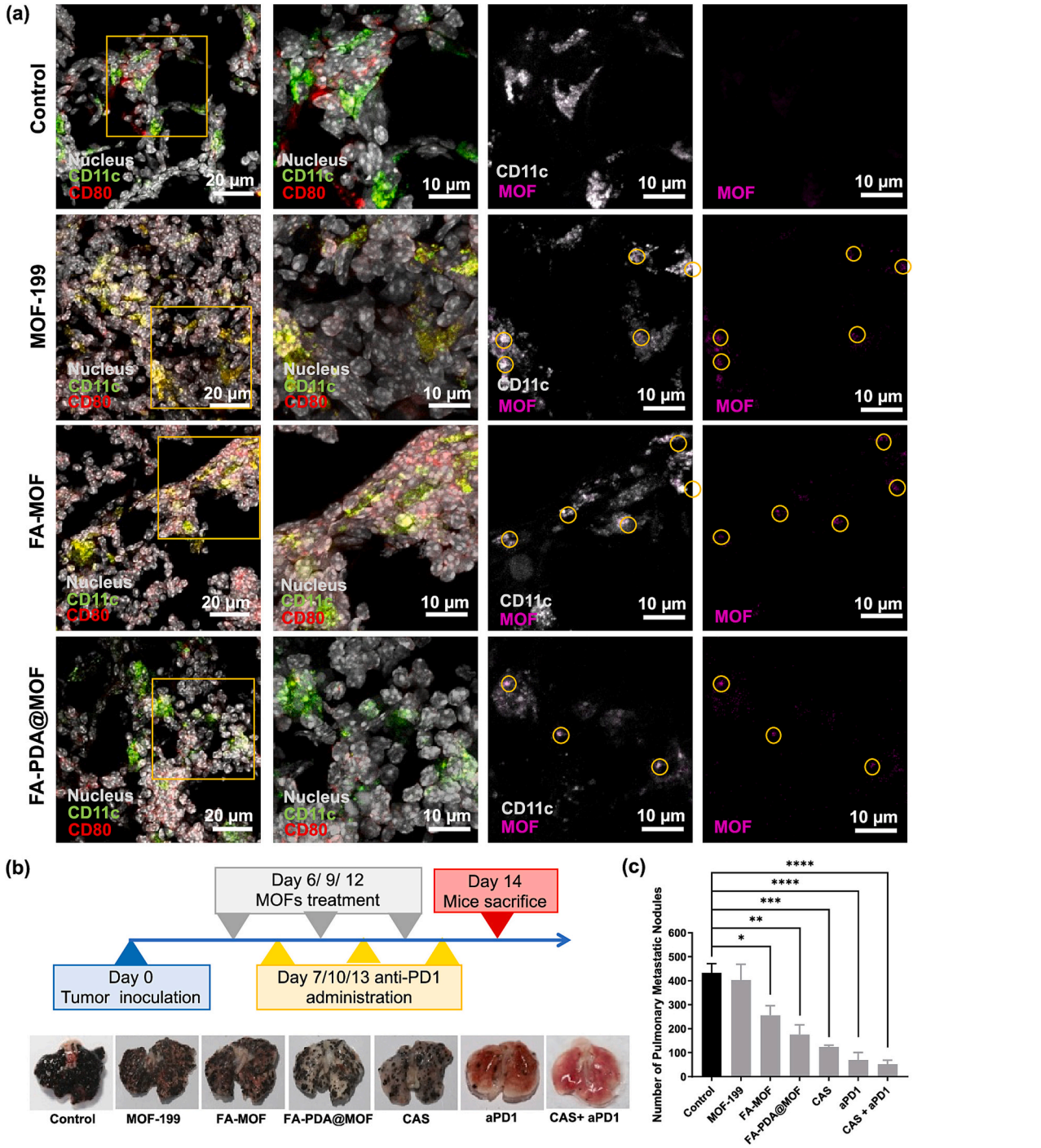

Fig. 9. *In vivo* efficacy study. (a) The confocal images for MOF at lymph node and staining with dendritic cell markers. (b) The therapeutic process for MOF and immune checkpoint inhibitor treatment. (c) Number of lung metastatic nodules was significantly reduced in the PDA-coated, CQ inhibition, and immunotherapy combining therapy group. Statistical significance was assessed using one-way ANOVA. Data represent mean ± SEM, *p < 0.05, **p < 0.01, ***p < 0.001.

cells to tumors organize (Fig. 7c, d). We propose that PDA can control and maintain the release of ROS and loaded drugs, can break the tight junction between tumor cells, and its antigen-capturing ability can train immune cells to specifically target tumor cells. Furthermore, T cell infiltration in healthy lung tissue was also evaluted. However, as normal lung tissue is not as densely populated as the tumor area, T cell infiltration is not significant (Fig. S9). These results demonstrate the potential of the CAS as a promising carrier for immunotherapeutic applications.

3.10. Antigens capture by catalytic antigen-capture sponge (CAS) trigger immune response

To investigate the underlying mechanism of T cell infiltration, the antigen capture ability was analyzed. To assess the ability of CAS to capture tumor antigens, CAS was incubated with B16F10 cell lysates. The successful capture of tumor antigens was confirmed by quantifying the total amount of protein bound by the CAS formulation using LC/MS/MS. The analysis revealed that 273 proteins were bound by CAS, with most of them being translational proteins (Fig. 8a). To further determine

the nature of these captured-proteins, we investigated their functions, specifically to distinguish between neoantigens expressed by B16F10 cells and damage-associated molecular patterns (DAMPs) that may elicit an immune response [50–52,75]. Neoantigens are unique antigens that are specific to tumors and are generated from somatic mutations. Our results indicate that Actn4, Eef2, and Rp113a, which had been reported as neoantigens, were captured by CAS [50–52]. Additionally, our results also showed that the CAS was able to capture several DAMPs, including heat shock proteins, histone proteins, and alarmins (HMGB1) (Fig. 8b). DAMPs are a diverse group of pro-inflammatory molecules that have been demonstrated to enhance immune responses. These findings confirm that CAS can effectively capture tumor-associated antigens, thereby further promoting immune activation. Furthermore, to verify the effect of serum proteins, the *in vitro* antigen capture assay with the incubation of CAS with serum collected from tumor-bearing mice was conducted before it interacts with B16F10 cells. The LC-MSMS results (Fig. S10) demonstrate that the CAS retains its effective antigen capture ability even after non-specific interactions with serum proteins.

Next, we aim to evaluate the ability of the CAS to be transported to the lymph node, an immune organ, and activate dendritic cells. Dendritic cells serve as antigen-presenting cells and have the capability to instruct cytotoxic T cells to specifically target and eliminate tumor cells. To assess the potential of the MOF to trigger an immune response, we conducted immunofluorescence staining of the lymph node and lung (Fig. 9a, S11). The results of CD80 and CD11c staining indicated that the MOF were able to be captured by mature dendritic cells [76]. This combined with the results from LC/MS/MS analysis suggests that the antigen-captured CAS has the potential to enhance the immune response and eradicate tumors.

3.11. Therapeutic efficacy of the combination of CAS and immunotherapy

Syngeneic lung-metastasis tumor mice model was used to evaluate the potential of MOFs to improve the efficacy of immunotherapy. Specifically, B16F10 melanoma lung cancer mice were treated with MOF and an anti-PD-1 (aPD-1) immune checkpoint inhibitor. 14 days after tumor inoculation, mice were euthanized and their lung tissues were examined to quantify the number of foci (Fig. 9b,c). The treatment effect was directly observed by a reduction in the number of B16F10 melanoma clusters isolated from the lung surface. This observation was further supported by the results of the survival study (Fig. S12). Therapeutic efficacy was gradually improved from MOF to FA-MOF and FA-PDA@MOF, which enabled complete targeting of lung metastatic tumor regions by exploiting FA conjugation for active targeting and PDA shell stability and antigen capture ability. Furthermore, the combination therapy of CAS and anti-PD1 showed significant synergy, suggesting that CAS has the potential to enhance immunotherapy through a combination of redox potential imbalance, autophagy inhibition, and immune stimulation. These findings suggest that CAS has promising value in combination with immune checkpoint inhibitors to improve immunotherapy outcomes. Moreover, to assess the potential hepatotoxicity the levels of alanine transaminase (ALT), albumin (ALB), and blood urea nitrogen (BUN), as well as conducted HE staining on liver were evaluated after the treatment with MOFs. In Fig. S13, the results indicated that the tested formulation did not exhibit any signs of liver toxicity.

4. Conclusions

In summary, a catalytic antigen-capture sponge (CAS) containing a copper-based metal organic framework (MOF) and chloroquine (CQ) has shown promise in programming T cell infiltration and inhibiting metastases in preclinical studies. The CAS is able to accumulate in tumors and induces chemodynamic therapy (CDT) *via* a Fenton-like reaction, leading to reduced levels of glutathione (GSH) and inhibition of autophagy. The CAS also acts as an antigen sponge, delivering tumor-associated antigens to dendritic cells and facilitating sustained immune stimulation. These treatments have the potential to overcome the immune privilege and heterogeneity of tumors, and the *in-situ* forming CAS lung metastasis as a CDT-induced antigen reservoir may lead to the infiltration of immune cells in metastatic clusters and inhibition of metastases. Further studies are needed to evaluate the safety and efficacy of this approach in humans.

CRediT authorship contribution statement

Min-Ren Chiang: Writing – original draft, Validation, Software, Methodology, Investigation, Formal analysis, Data curation, Conceptualization. **Wei-Ting Shen:** Writing – original draft, Visualization, Project administration, Methodology, Investigation, Formal analysis, Data curation, Conceptualization. **Pin-Xuan Huang:** Validation, Software, Project administration, Formal analysis, Data curation, Conceptualization. **Kang-Li Wang:** Writing – original draft, Validation, Software, Formal analysis, Data curation. **Wei-Han Weng:** Resources, Methodology, Investigation, Data curation. **Chien-Wen Chang:** Validation, Supervision, Project administration, Methodology, Data curation. **Wen-Hsuan Chiang:** Visualization, Supervision, Software, Resources, Methodology, Investigation, Funding acquisition. **Yu-Chen Liu:** Validation, Supervision, Software, Methodology, Data curation. **Shing-Jyh Chang:** Visualization, Supervision, Resources, Methodology, Formal analysis. **Shang-Hsiu Hu:** Writing – review & editing, Visualization, Validation, Supervision, Software, Resources, Formal analysis.

Declaration of Competing Interest

The authors declare no conflict of interest.

Data availability

The data that support the findings of this study are available within the article and its supporting information

Acknowledgments

This work was financially supported by the National Science and Technology Council, Taiwan under contracts MOST 111-2314-B-007-003-MY3, MOST 111-2636-E-007-021 and MOST-110-2634-F-007-025, National Tsing Hua University (111Q2715E1 and 111F7MELE1) and National Health Research Institutes (NHRI-EX112-11111EI) in Taiwan. The authors acknowledge the mass spectrometry technical research services from Consortia of Key Technologies and Instrumentation Center, National Taiwan University.

Appendix A. Supplementary data

Supplementary data to this article can be found online at https://doi.org/10.1016/j.jconrel.2023.06.033.

References

[1] R.L. Siegel, K.D. Miller, H.E. Fuchs, A. Jemal, Cancer statistics, 2021, CA Cancer J. Clin. 71 (2021) 7–33.
[2] Y.R. Murciano-Goroff, A.B. Warner, J.D. Wolchok, The future of cancer immunotherapy: microenvironment-targeting combinations, Cell Res. 30 (2020) 507–519.
[3] W. Park, Y.J. Heo, D.K. Han, New opportunities for nanoparticles in cancer immunotherapy, Biomater. Res. 22 (2018) 24.
[4] C.M. Neophytou, M. Panagi, T. Stylianopoulos, P. Papageorgis, The role of tumor microenvironment in cancer metastasis: molecular mechanisms and therapeutic opportunities, Cancers (Basel) 13 (2021) 2053.
[5] B.N. Yalamandala, T.M.H. Huynh, M.R. Chiang, W.H. Weng, C.W. Chang, W. H. Chiang, S.H. Hu, Programmed catalytic therapy and antigen capture-mediated dendritic cells harnessing cancer immunotherapies by in situ-forming adhesive nanoreservoirs, Adv. Funct. Mater. 2210644 (2022).

[6] W.T. Shen, R.S. Hsu, J.H. Fang, P.F. Hu, C.S. Chiang, S.H. Hu, Marginative delivery-mediated extracellular leakiness and T cell infiltration in lung metastasis by a biomimetic nanoraspberry, Nano Lett. 21 (2021) 1375–1383.

[7] E. Blanco, H. Shen, M. Ferrari, Principles of nanoparticle design for overcoming biological barriers to drug delivery, Nat. Biotechnol. 33 (2015) 941–951.

[8] Y. Zhang, F.M. Wang, E.G. Ju, Z. Liu, Z.W. Chen, J.S. Ren, X.G. Qu, Metal-organic-framework-based vaccine platforms for enhanced systemic immune and memory response, Adv. Funct. Mater. 26 (2016) 6454–6461.

[9] M.R. Chiang, Y.L. Su, C.Y. Chang, C.W. Chang, S.H. Hu, Lung metastasis-targeted donut-shaped nanostructures shuttled by the margination effect for the PolyDox generation-mediated penetrative delivery into deep tumors, Mater. Horiz. 7 (2020) 1051–1061.

[10] C. Liu, X. Liu, X.C. Xiang, X. Pang, S.Y. Chen, Y.M. Zhang, E. Ren, L.L. Zhang, X. Liu, P. Lv, X.Y. Wang, W.X. Luo, N.S. Xia, X.Y. Chen, G. Liu, A nanovaccine for antigen self-presentation and immunosuppression reversal as a personalized cancer immunotherapy strategy, Nat. Nanotechnol. 17 (2022) 531–540.

[11] Q.X. Zhang, S.S. Li, J.D. Ren, X. He, H.K. Shi, F.H. Zhang, H. Li, R.S. Tong, ROS-triggered nanoinducer based on dermatan sulfate enhances immunogenic cell death in melanoma, J. Control. Release 348 (2022) 22–33.

[12] M.L. Zhou, C.H. Luo, Z. Zhou, L. Li, Y. Huang, Improving anti-PD-L1 therapy in triple negative breast cancer by polymer-enhanced immunogenic cell death and CXCR4 blockade, J. Control. Release 334 (2021) 248–262.

[13] E. Saito, S.J. Gurczynski, K.R. Kramer, C.A. Wilke, S.D. Miller, B.B. Moore, L. D. Shea, Modulating lung immune cells by pulmonary delivery of antigen-specific nanoparticles to treat autoimmune disease, Sci. Adv. 6 (2020) 9317.

[14] Q. Wang, Z. Wang, X.X. Sun, Q.K. Jiang, B.J. Sun, Z.G. He, S.W. Zhang, C. Luo, J. Sun, Lymph node-targeting nanovaccines for cancer immunotherapy, J. Control. Release 351 (2022) 102–122.

[15] G.B. Kim, H.D. Sung, G.H. Nam, W. Kim, S. Kim, D. Kang, E.J. Lee, I.S. Kim, Design of PD-1-decorated nanocages targeting tumor-draining lymph node for promoting T cell activation, J. Control. Release 333 (2021) 328–338.

[16] Y.H. You, Y.F. Lin, B. Nirosha, H.T. Chang, Y.F. Huang, Polydopamine-coated gold nanostar for combined antitumor and antiangiogenic therapy in multidrug-resistant breast cancer, Nanotheranostics 3 (2019) 266–283.

[17] A. Mpakali, E. Stratikos, The role of antigen processing and presentation in cancer and the efficacy of immune checkpoint inhibitor immunotherapy, Cancers 13 (2021) 134.

[18] J. Huang, B. Yang, Y. Peng, J.S. Huang, S.H.D. Wong, L.M. Bian, K.S. Zhu, X. T. Shuai, S.S. Han, Nanomedicine-boosting tumor immunogenicity for enhanced immunotherapy, Adv. Funct. Mater. 31 (2021) 2011171.

[19] J.W. Wang, J. Wang, J.J. Xu, T. Hou, L. Yin, H. Chen, Y. Ma, W.T. Chen, Z.Y. Wang, Y.L. Hou, Y. Ding, Anchoring a xenogeneic antigen-guided immune activation system to tumor cell membrane for solid tumor treatment, Adv. Funct. Mater. 32 (2022) 2111499.

[20] L. Guo, R.X. Wei, R. Sun, Q. Yang, G.J. Li, L.Y. Wang, H.B. Luo, M. Feng, "Cytokine-microfactories" recruit DCs and deliver tumor antigens via gap junctions for immunotherapy, J. Control. Release 337 (2021) 417–430.

[21] J. Li, J. Li, Y. Peng, Y. Du, Z. Yang, X. Qi, Dendritic cell derived exosomes loaded neoantigens for personalized cancer immunotherapies, J. Control. Release 353 (2023) 423–433.

[22] Q. Cheng, F. Gao, W.Y. Yu, M.Z. Zou, X.L. Ding, M.J. Li, S.X. Cheng, X.Z. Zhang, Near-infrared triggered cascade of antitumor immune responses based on the integrated core-shell nanoparticle, Adv. Funct. Mater. 30 (2020) 2000335.

[23] W. Liu, M. Ota, M. Tabushi, Y. Takahashi, Y. Takakura, Development of allergic rhinitis immunotherapy using antigen-loaded small extracellular vesicles, J. Control. Release 345 (2022) 433–442.

[24] C. Liu, L. Li, J. Lyu, Y. Xiang, L. Chen, Z. Zhou, Y. Huang, Split bullets loaded nanoparticles for amplified immunotherapy, J. Control. Release 347 (2022) 199–210.

[25] Y. Chi, J. Remsik, V. Kiseliovas, C. Derderian, U. Sener, M. Alghader, F. Saadeh, K. Nikishina, T. Bale, C. Iacobuzio-Donahue, T. Thomas, D. Pe'er, L. Mazutis, A. Boire, Cancer cells deploy lipocalin-2 to collect limiting iron in leptomeningeal metastasis, Science 369 (2020) 276.

[26] Q. Li, Y. Liu, Y.R. Zhang, W. Jiang, Immunogenicity-boosted cancer immunotherapy based on nanoscale metal-organic frameworks, J. Control. Release 347 (2022) 183–198.

[27] W. Cheng, Y.L. Su, H.H. Hsu, Y.H. Lin, L.A. Chu, W.C. Huang, Y.J. Lu, C.S. Chiang, S.H. Hu, Rabies virus glycoprotein-mediated transportation and t cell infiltration to brain tumor by magnetoelectric gold yarnballs, ACS Nano 16 (2022) 4014–4027.

[28] Y. Jiang, N. Krishnan, J.R. Zhou, S. Chekuri, X.L. Wei, A.V. Kroll, C.L. Yu, Y. O. Duan, W.W. Gao, R.N.H. Fang, L.F. Zhang, Engineered cell-membrane-coated nanoparticles directly present tumor antigens to promote anticancer immunity, Adv. Mater. 32 (2020) 2001808.

[29] S. Koo, O.K. Park, J. Kim, S.I. Han, T.Y. Yoo, N. Lee, Y.G. Kim, H. Kim, C. Lim, J. S. Bae, J. Yoo, D. Kim, S.H. Choi, T. Hyeon, Enhanced chemodynamic therapy by Cu-Fe peroxide nanoparticles: tumor microenvironment-mediated synergistic Fenton reaction, ACS Nano 16 (2022) 2535–2545.

[30] S. Sheng, F. Liu, L. Lin, N. Yan, Y.B. Wang, C.N. Xu, H.Y. Tian, X.S. Chen, Nanozyme-mediated cascade reaction based on metal-organic framework for synergetic chemo-photodynamic tumor therapy, J. Control. Release 328 (2020) 631–639.

[31] G. Lee, C.W. Kim, J.R. Choi, K.H. Min, H.J. Lee, K.H. Kwack, H.W. Lee, J.H. Lee, S. Y. Jeong, K. Chang, S.C. Lee, Copper arsenite-complexed Fenton-like nanoparticles as oxidative stress-amplifying anticancer agents, J. Control. Release 341 (2022) 646–660.

[32] B.N. Yalamandala, P.H. Chen, T. Moorthy, T.M.H. Huynh, W.H. Chiang, S.H. Hu, Programmed catalytic therapy-mediated ROS generation and T-cell infiltration in lung metastasis by a dual metal-organic framework (MOF) nanoagent, Pharmaceutics 14 (2022) 527.

[33] L.S. Lin, J.B. Song, L. Song, K.M. Ke, Y.J. Liu, Z.J. Zhou, Z.Y. Shen, J. Li, Z. Yang, W. Tang, G. Niu, H.H. Yang, X.Y. Chen, Simultaneous Fenton-like ion delivery and glutathione depletion by MnO_2-based nanoagent to enhance chemodynamic therapy, Angew. Chem. Int. Ed. 57 (2018) 4902–4906.

[34] B. Nirosha Yalamandala, W.T. Shen, S.H. Min, W.H. Chiang, S.J. Chang, S.H. Hu, Advances in functional metal-organic frameworks based on-demand drug delivery systems for tumor therapeutics, Adv. NanoBiomed Res. 1 (2021) 2100014.

[35] E. White, Deconvoluting the context-dependent role for autophagy in cancer, Nat. Rev. Cancer 12 (2012) 401–410.

[36] L. Rivas-Garcia, J.L. Quiles, A. Varela-Lopez, F. Giampieri, M. Battino, J. Bettmer, M. Montes-Bayon, J. Llopis, C. Sanchez-Gonzalez, Ultra-small iron nanoparticles target mitochondria inducing autophagy, acting on mitochondrial DNA and reducing respiration, Pharmaceutics 13 (2021) 90.

[37] X.X. Wang, M.M. Shang, X. Sun, L. Guo, S. Xiao, D.D. Shi, D. Meng, Y.D. Zhao, L. Z. Yang, C. Jiang, J. Li, Dual-responsive nanodroplets combined with ultrasound-targeted microbubble destruction suppress tumor growth and metastasis *via* autophagy blockade, J. Control. Release 343 (2022) 66–77.

[38] J.W. Dong, C.F. Zhu, F.R. Zhang, Z.W. Zhou, M.J. Sun, "Attractive/adhesion force" dual-regulatory nanogels capable of CXCR4 antagonism and autophagy inhibition for the treatment of metastatic breast cancer, J. Control. Release 341 (2022) 892–903.

[39] M. Mauthe, I. Orhon, C. Rocchi, X.D. Zhou, M. Luhr, K.J. Hijlkema, R.P. Coppes, N. Engedal, M. Mari, F. Reggiori, Chloroquine inhibits autophagic flux by decreasing autophagosome-lysosome fusion, Autophagy 14 (2018) 1435–1455.

[40] H.X. Ye, M.T. Chen, F. Cao, H.G. Huang, R.Y. Zhan, X.J. Zheng, Chloroquine, an autophagy inhibitor, potentiates the radiosensitivity of glioma initiating cells by inhibiting autophagy and activating apoptosis, BMC Neurol. 16 (2016) 178.

[41] Y. Chao, Q. Chen, Z. Liu, Smart injectable hydrogels for cancer immunotherapy, Adv. Funct. Mater. 30 (2020) 1902785.

[42] H.Y. Ma, C.L. He, X.S. Chen, Injectable hydrogels as local depots at tumor sites for antitumor immunotherapy and immune-based combination therapy, Macromol. Biosci. 21 (2021) 2100039.

[43] Q. Li, Z.P. Zhao, X.H. Qin, M.Z. Zhang, Q. Du, Z.H. Li, Y.X. Luan, A checkpoint-regulatable immune niche created by injectable hydrogel for tumor therapy, Adv. Funct. Mater. 31 (2021) 2104630.

[44] P.M.P. Ferreira, R.W.R. Sousa, J.R.O. Ferreira, G.C.G. Militao, D.P. Bezerra, Chloroquine and hydroxychloroquine in antitumor therapies based on autophagy-related mechanisms, Pharmacol. Res. 168 (2021), 105582.

[45] S. Chen, C. Wang, M. Zhang, W. Zhang, J. Qi, X. Sun, L. Wang, J. Li, N-doped cu-MOFs for efficient electrochemical determination of dopamine and sulfanilamide, J. Hazard. Mater. 390 (2020), 122157.

[46] Y. Jeong, D.G. Jwa, A. You, S. Park, J.G. Kim, S.M. Kang, M. Kim, Photochemical control of polydopamine coatinginan aprotic organic solvent, Asian, J. Organomet. Chem. 8 (2019) 1610–1612.

[47] Y.X. Tu, C.F. Lei, F. Deng, Y. Chen, Y. Wang, Z.K. Zhang, Core-shell ZIF-8@ polydopamine nanoparticles obtained by mitigating the polydopamine coating induced self-etching of MOFs: prototypical metal ion reservoirs for sticking to and killing bacteria, New J. Chem. 45 (2021) 8701–8713.

[48] B.N. Khlebtsov, A.M. Burov, T.E. Pylaev, N.G. Khlebtsov, Polydopamine-coated Au nanorods for targeted fluorescent cell imaging and photothermal therapy, Beilstein J. Nanotechnol. 10 (2019) 794–803.

[49] Y. Zhao, Q. Yang, C.X. Jin, Y.F. Feng, S.H. Xie, H.Y. Xie, Y.W. Qi, H.N. Qiu, H. Y. Chen, A.L. Tao, J.B. Mu, W.J. Qin, J. Huang, Changes of CD103-expressing pulmonary CD4(+) and CD8(+) T cells in S. japonicum infected C57BL/6 mice, Bmc, Infect. Dis. Ther. 19 (2019) 999.

[50] S. Kreiter, M. Vormehr, N. van de Roemer, M. Diken, M. Lower, J. Diekmann, S. Boegel, B. Schrors, F. Vascotto, J.C. Castle, A.D. Tadmor, S.P. Schoenberger, C. Huber, O. Tureci, U. Sahin, Mutant MHC class II epitopes drive therapeutic immune responses to cancer, Nature 520 (2015) 692–696.

[51] Y. Min, K.C. Roche, S. Tian, M.J. Eblan, K.P. McKinnon, J.M. Caster, S. Chai, L. E. Herring, L. Zhang, T. Zhang, J.M. DeSimone, J.E. Tepper, B.G. Vincent, J. S. Serody, A.Z. Wang, Antigen-capturing nanoparticles improve the abscopal effect and cancer immunotherapy, Nat. Nanotechnol. 12 (2017) 877–882.

[52] J.C. Castle, S. Kreiter, J. Diekmann, M. Lower, N. van de Roemer, J. de Graaf, A. Selmi, M. Diken, S. Boegel, C. Paret, M. Koslowski, A.N. Kuhn, C.M. Britten, C. Huber, O. Tureci, U. Sahin, Exploiting the mutanome for tumor vaccination, Cancer Res. 72 (2012) 1081–1091.

[53] R.L. Schroeder, J.P. Gerber, Chloroquine and hydroxychloroquine binding to melanin: some possible consequences for pathologies, Toxicol. Rep. 1 (2014) 963–968.

[54] T. He, W. Zhu, X. Wang, P. Yu, S. Wang, G. Tan, C. Ning, Polydopamine assisted immobilisation of copper(II) on titanium for antibacterial applications, Mater. Technol. 30 (2015) B68–B72.

[55] X. Yu, H. Fan, L. Wang, Z. Jin, Formation of polydopamine nanofibers with the aid of folic acid, Angew. Chem. Int. Ed. Eng. 53 (2014) 12600–12604.

[56] X. Li, H.L. Liu, X.S. Jia, G.Y. Li, T.C. An, Y.P. Gao, Novel approach for removing brominated flame retardant from aquatic environments using Cu/Fe-based metal-organic frameworks: a case of hexabromocyclododecane (HBCD), Sci. Total Environ. 621 (2018) 1533–1541.

[57] X.N. Chen, X.H. Wang, D. Fang, A review on C1s XPS-spectra for some kinds of carbon materials, Fuller. Nanotub. Car. N 28 (2020) 1048–1058.

[58] B.F. Shi, Y.B. Su, Y. Duan, S.Y. Chen, W.Y. Zuo, A nanocomposite prepared from copper(II) and nitrogen-doped graphene quantum dots with peroxidase mimicking properties for chemiluminescent determination of uric acid, Microchim. Acta 186 (2019) 397.
[59] H.P. Zhang, W. Han, J. Tavakoli, Y.P. Zhang, X.Y. Lin, X. Lu, Y. Ma, Y.H. Tang, Understanding interfacial interactions of polydopamine and glass fiber and their enhancement mechanisms in epoxy-based laminates, Compos. Part A-Appl. S 116 (2019) 62–71.
[60] J. Manna, S. Akbayrak, S. Ozkar, Palladium(0) nanoparticles supported on polydopamine coated Fe3O4 as magnetically isolable, highly active and reusable catalysts for hydrolytic dehydrogenation of ammonia borane, RSC Adv. 6 (2016) 102035–102042.
[61] S.L. Yang, L. Peng, D.T. Sun, M. Asgari, E. Oveisi, O. Trukhina, S. Bulut, A. Jamali, W.L. Queen, A new post-synthetic polymerization strategy makes metal-organic frameworks more stable, Chem. Sci. 10 (2019) 4542–4549.
[62] R. Batul, M. Bhave, P.J. Mahon, A. Yu, Polydopamine nanosphere with *in-situ* loaded gentamicin and its antimicrobial activity, Molecules 25 (2020) 2090.
[63] M.Z. Mohammadabad, M. Moeinaddini, M. Nowrouzi, R. Rafiee, A. Abbasi, Facile and cost-efficient synthesis of highly efficient CO2 adsorbents: a pathway towards a green environment, J. Porous. Mater. 27 (2020) 1659–1668.
[64] T. Sonstevold, N. Engedal, M.L. Torgersen, Perturbation of cellular redox homeostasis dictates divergent effects of polybutyl cyanoacrylate (PBCA) nanoparticles on autophagy, Cells 10 (2021) 3432.
[65] Y. Chen, B. Wang, X.Q. Wang, L.H. Xie, J.P. Li, Y.B. Xie, J.R. Li, A copper(II)-paddlewheel metal-organic framework with exceptional hydrolytic stability and selective adsorption and detection ability of aniline in water, ACS Appl. Mater. Interfaces 9 (2017) 27027–27035.
[66] J. Qu, D. Guillory, P. Cheah, B. Tian, J. Zheng, Y.J. Liu, C. Cates, A.V. Janorkar, Y. F. Zhao, Synthesis of biomimetic melanin-like multifunctional nanoparticles for ph responsive magnetic resonance imaging and photothermal therapy, Nanomaterials (Basel) 11 (2021) 2107.
[67] Y. Chen, O. Tezcan, D. Li, N. Beztsinna, B. Lou, T. Etrych, K. Ulbrich, J. M. Metselaar, T. Lammers, W.E. Hennink, Overcoming multidrug resistance using folate receptor-targeted and pH-responsive polymeric nanogels containing covalently entrapped doxorubicin, Nanoscale 9 (2017) 10404–10419.
[68] R. Chen, C. Zhu, Y. Fan, W. Feng, J. Wang, E. Shang, Q. Zhou, Z. Chen, Polydopamine-based multifunctional platform for combined photothermal therapy, chemotherapy, and immunotherapy in malignant tumor treatment, ACS Appl. Bio Mater. 2 (2019) 874–883.
[69] B.W. Yang, L. Ding, H.L. Yao, Y. Chen, J.L. Shi, A metal-organic framework (mof) fenton nanoagent-enabled nanocatalytic cancer therapy in synergy with autophagy inhibition, Adv. Mater. 32 (2020) 1907152.
[70] L. Galluzzi, J.M. Bravo-San Pedro, B. Levine, D.R. Green, G. Kroemer, Pharmacological modulation of autophagy: therapeutic potential and persisting obstacles, Nat. Rev. Drug Discov. 16 (2017) 487–511.
[71] Y. Nakamura, A. Mochida, P.L. Choyke, H. Kobayashi, Nanodrug delivery: is the enhanced permeability and retention effect sufficient for curing cancer? Bioconjug. Chem. 27 (2016) 2225–2238.
[72] J.A. Ledermann, S. Canevari, T. Thigpen, Targeting the folate receptor: diagnostic and therapeutic approaches to personalize cancer treatments, Ann. Oncol. 26 (2015) 2034–2043.
[73] M.L. Circu, T.Y. Aw, Reactive oxygen species, cellular redox systems, and apoptosis, Free Radic. Biol. Med. 48 (2010) 749–762.
[74] D.G. Chen, J. Xie, R. Fiskesund, W.Q. Dong, X.Y. Liang, J.D. Lv, X. Jin, J.Y. Liu, S. Q. Mo, T.Z. Zhang, F.R. Cheng, Y.B. Zhou, H.F. Zhang, K. Tang, J.W. Ma, Y.Y. Liu, B. Huang, Chloroquine modulates antitumor immune response by resetting tumor-associated macrophages toward M1 phenotype, Nat. Commun. 9 (2018) 873.
[75] D.V. Krysko, A.D. Garg, A. Kaczmarek, O. Krysko, P. Agostinis, P. Vandenabeele, Immunogenic cell death and DAMPs in cancer therapy, Nat. Rev. Cancer 12 (2012) 860–875.
[76] S. Dilioglou, J.M. Cruse, R.E. Lewis, Function of CD80 and CD86 on monocyte- and stem cell-derived dendritic cells, Exp. Mol. Pathol. 75 (2003) 217–227.